Supporting Information

A comprehensive evaluation of the temporal and spatial fouling characteristics of RO membranes in a full-scale seawater desalination plant

Chao Chen[a], Yu Yang[a,*], Nigel J.D. Graham[b], Zhenyu Li[c], Xingtao Yang[d], Zhining Wang[e], Nadia Farhat[f], Johannes S. Vrouwenvelder[f], Li-an Hou[a]

[a]State Key Laboratory of Water Environment Simulation, School of Environment, Beijing Normal University, Beijing 100875, China

[b]Department of Civil and Environmental Engineering, Imperial College London, South Kensington Campus, London SW7 2AZ, UK

[c]College of Food Science and Engineering, Northwest A&F University, Yangling, Shaanxi 712100, PR China

[d]Qingdao Bcta Desalination Co., Ltd, Qingdao, 266100, China

[e]Shandong Provincial Key Laboratory of Water Pollution Control and Resource Reuse, School of Environmental Science and Engineering, Shandong University, Qingdao 266237, China

[f]Water Desalination and Reuse Center (WDRC), Biological and Environmental Science & Engineering (BESE) Division, King Abdullah University of Science and Technology (KAUST), Thuwal 23955-6900, Saudi Arabia

[*] Corresponding author: Yu Yang

Email address: yangyu@bnu.edu.cn

Contents

Method S1. Analytical methods

The protein and polysaccharide concentrations were determined by the Bradford method (BCA Protein Assay Kit, Thermo Scientific, USA) and phenol-H_2SO_4 method (Li et al., 2018), respectively. Total organic carbon (TOC) analysis was performed using a TOC-VCSH analyzer (Shimadzu, Boulder, CO, USA). Adenosine triphosphate (ATP) content measurements were carried out using BacTiter-Glo microbial viability assay kit (Promega, USA) and 96-well luminometer (Sigma Aldrich) at room temperature within 15 min. EEM analysis was performed from 200 to 450 nm for excitation spectra and 250 to 550 nm for emission spectra at 5-nm intervals (F-4600, Hitachi, Japan). After normalization of the results of the excitation-emission matrix (EEM), samples extracted from the foulant membrane and spacer surface were subjected to analysis of the EEM-parallel factor (EEM-PARAFAC) (Method S3). The biofilms on the fouled membranes were stained with SYTO9 (ex 480/em 500)/PI (ex 490/em 635) to detect live and dead cells and were observed using a confocal laser scanning microscope (CLSM) based on the methods of previous studies (Li et al., 2018). The fluorescence intensities of the live cells (500 nm emission (green)) and dead cells (635 nm emission (red)) were evaluated by ImageJ (Li et al., 2018). Thermo Scientific™ Dionex™ ion chromatography (IC) and Perkin Elmer OPTIMA 7300 inductively coupled plasma-optical emission spectroscopy (ICP–OES) were used for inorganic element analysis.

Method S2. Material and chemicals

The following reagents and materials were employed to characterize the biofilm: sodium

hydroxide (NaOH, Sinopharm, 98%), phenol (C_6H_5OH, Xi-long, 99%), sulfuric acid (H_2SO_4, Sinopharm, 98%), 96-well luminometer (Sigma Aldrich), bicinchoninic acid assay kit (BCA Protein Assay Kit, Thermo Scientific, USA), BacTiter-Glo microbial viability assay kit (Promega, USA), TIANSeq DirectFast DNA Library Prep Kit (illumine) (TIANGEN BIOTECH Co., Ltd., Beijing, China), and SYTO9 and propidium iodide (LIVE/DEAD Baclight Bacterial Viability Kit, Life Technologies Corporation). Nonradioactive isotopes of cesium nitrate ($CsNO_3$) and strontium nitrate ($Sr(NO_3)_2$) were obtained from Acros (America) and Alfa Aesar (China).

Method S3. Parallel factor modeling of an excitation-emission matrix (EEM-PARAFAC)

EEM analysis was performed from 200 to 450 nm for excitation spectra and 250 to 550 nm for emission spectra at 5-nm intervals (F-4600, Hitachi, Japan). After normalization of the EEM results, samples extracted from the foulant membrane and spacer surface were subjected to EEM-PARAFAC analysis (Wu et al., 2020; Yu et al., 2010). EEM-PARAFAC analysis was used to decompose the complex fluorescence signals obtained by EEM analysis into several chemically independent fluorescence components (Yu et al., 2010). The datasets were modeled using the DOMFluor toolbox (Stedmon and Bro, 2008) in MATLAB_R2019b. All EEM data were normalized prior to PARAFAC modeling. The preliminary models with 2 to 5 components were computed in the exploratory analysis before determining the number of EEM components based on the visual investigation, residual analysis, and split-half validation (Xu et al., 2022). The Fmax (R.U.) value of each FDOM component was assigned to be the highest fluorescence and used as a relative concentration to represent the FDOM quantity.

Method S4. 16S rRNA sequencing analysis and microbial community analysis

Basically, DNA was extracted from biofilm samples using a TIANSeq DirectFast DNA Library Prep Kit (illumine) (TIANGEN BIOTECH Co., Ltd., Beijing, China) according to the manufacturer's protocol. After extraction, electrophoresis (1% agarose gel, 5 V/cm, 20 min) and spectrophotometers were employed to check genomic DNA, which was subsequently stored at −20 °C until further research. The hypervariable region V3–V4 of the segment in the bacterial 16S rRNA was amplified by polymerase chain reaction (PCR) with the fusion primer set 338F (*5′-AC TCCTACGGGAGGCAGCAG-3′*)/806R (*5′-GGACTACNNGGG TATCTAAT-3′*). The PCR products were quantified by the QuantiFluor™-ST blue fluorescence quantitative system (Promega, USA) and then sequenced using the Illumina MiSeq PE300 platform (Illumina, San Diego, USA) after a composite sequencing library was structured based on equimolar ratios of amplicons from all samples.

Operational taxonomic units (OTUs) with a 97% similar cutoff were identified using the UPARSE version 7.1 function within USEARCH (Edgar, 2013). Poor-quality reads and chimeric sequences were removed using USEARCH default settings. The taxonomy of each OTU representative sequence was classified using the Ribosomal database project database. Rarified OTU tables were used to generate alpha and beta diversity metrics (Belila et al., 2016). Bacterial diversity and linear discriminant analysis effect size were both performed using the free online platform of the Majorbio Cloud Platform (www.majorbio.com) (Ma et al., 2023). Bacterial community variation was analyzed with principal coordinate analysis (PCoA) in QIIME using

unweighted UniFrac distance matrix (Lozupone et al., 2011) and partial least squares discriminant analysis (PLS-DA) as measures of beta diversity. LEfSe analysis was used to compare the significant differences in bacterial composition between the different groups (Liu et al., 2020). A Kruskal–Wallis test was performed to calculate the significance P value in the LEfSe analysis, followed by multiple comparisons adjusted by false discovery rate (fdr). A P value < 0.05 indicated a significant difference.

Method S5. Performance evaluation and solution-diffusion model

The fouled membrane samples were first immersed for 30 min in each Na_4EDTA (0.1 wt% at pH = 11.0 adjusted using NaOH) with citric acid (0.1 wt%), followed by thorough rinsing with ultrapure water (Suzuki et al., 2016). Each laboratory-scale RO unit comprised a flat-sheet membrane cell with an effective membrane area of 140 cm^2 combined with shims, spacer, and carrier. The membrane samples were compacted at 5.5 MPa using ultrapure water until water permeation stabilized and tests were then performed at 2-5 MPa. The membrane flux and rejection were determined in a cross-flow filtration cell using 32,000 mg/L NaCl solutions containing 1 mg/L Cs^+ and Sr^{2+} as the feeds. A temperature of 25 ± 1 °C and pH = 6.5-7 were kept constant during all the experiments. The experiments evaluated both water flux and solute (salt, Cs^+, and Sr^{2+}) rejection. The concentration of salt was obtained by a conductometer, and the Cs^+ and Sr^{2+} concentrations were measured using inductively coupled plasma–mass spectroscopy (ICP–MS) analysis (Shimadzu ICP–MS 2030).

The membrane flux (J_v, m·day^{-1}) and rejection R (dimensionless) were determined from

Equations (S1) and (S2) (Urama and Marinas, 1997):

$$J_v = A(\Delta p - \Delta \pi) \tag{S1}$$

$$R = 1 - \frac{C_p}{C_f} \tag{S2}$$

where A, Δp, and $\Delta \pi$ represent the specific water permeability coefficient (m·MPa^{-1}·day^{-1}), transmembrane applied pressure (MPa), and transmembrane osmotic pressure (MPa), respectively. C_p and C_f represent the concentrations of the salt and radionuclide in the permeated and feed solutions, respectively.

The experimental results (water flux and solute (salt, Cs^+, and Sr^{2+}) rejection) were analyzed using the solution-diffusion model. Solute rejection R was expressed according to Eq. (S3).

$$R = \frac{1}{\left(\frac{a}{1-a} + \frac{B}{1-a}\frac{1}{J_v}\right)\exp\left(\frac{J_v}{k}\right) + 1} \tag{S3}$$

where B, a, and k represent the solute diffusive permeation coefficient in the active layer (m·day^{-1}), the advective permeation coefficient in the active layer (dimensionless), and the solute mass transfer coefficient in the concentration polarization layer adjacent to the membrane surface (Matthiasson and Sivik, 1980), respectively. For the case of high turbulence conditions in the feed solution channel (i.e., $k \approx \infty$ and $exp\left(\frac{J_v}{k}\right) \approx 1$) (see Method S6 and Fig. S16), the significance of the concentration polarization effect can be evaluated using Eq. (S4) as given by

$$R = \frac{1}{\frac{B}{1-a}\frac{1}{J_v} + \frac{1}{1-a}} \tag{S4}$$

Eq. (4) was employed for fitting solute diffusive (B) and advective (a) transport coefficients from J_v and R experimental data (Suzuki et al., 2016).

Method S6. Assessment of the importance of concentration polarization in permeation tests

The relatively high crossflow velocity was used to minimize concentration polarization and more accurately estimate water/solute transport parameters. The significance of the concentration polarization effect can be assessed by taking the reciprocal of Eq. (S4) as given by Eq. (S5) and plotting 1/R on the vertical axis and $1/J_v$ on the horizontal axis (Suzuki et al., 2016).

$$\frac{1}{R} = \left(\frac{a}{1-a} + \frac{B}{1-a}\frac{1}{J_v}\right) exp\left(\frac{J_v}{k}\right) + 1 \qquad (S5)$$

For the case of high turbulence conditions in the feed solution channel (i.e., $k \approx \infty$ and $exp\left(\frac{J_v}{k}\right) \approx 1$) (Matthiasson and Sivik, 1980), Eq. (S5) is simplified to

$$\frac{1}{R} = \left(\frac{a}{1-a} + \frac{B}{1-a}\frac{1}{J_v}\right) \qquad (S6)$$

which corresponds to a straight line having a slope of magnitude/(1-a) and intercept of 1/(1-a).
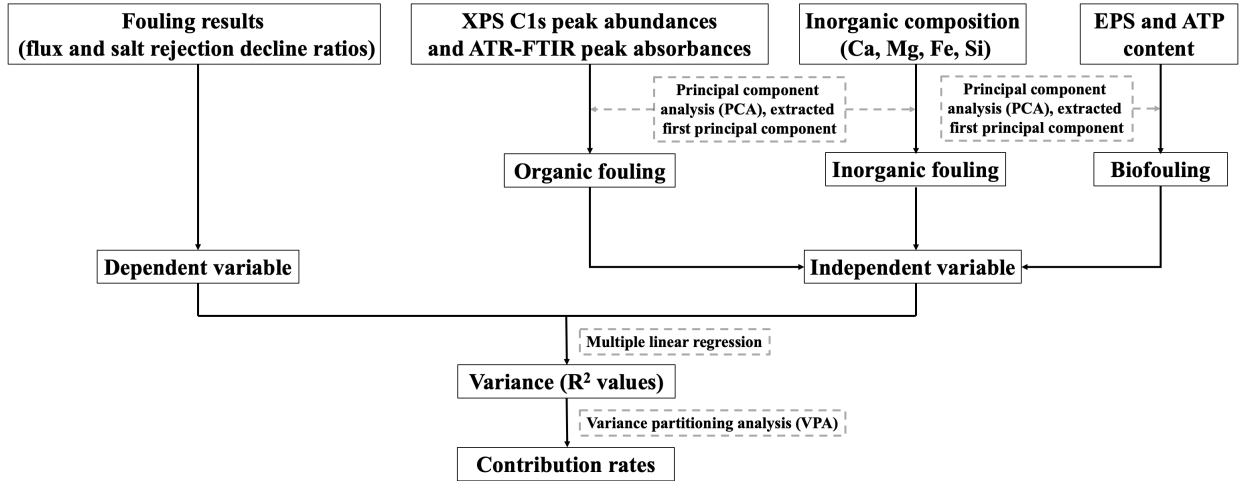
Fig. S1. Flow chart of variance partitioning analysis (VPA) in quantifying the individual and interactive contributions of different types of fouling.
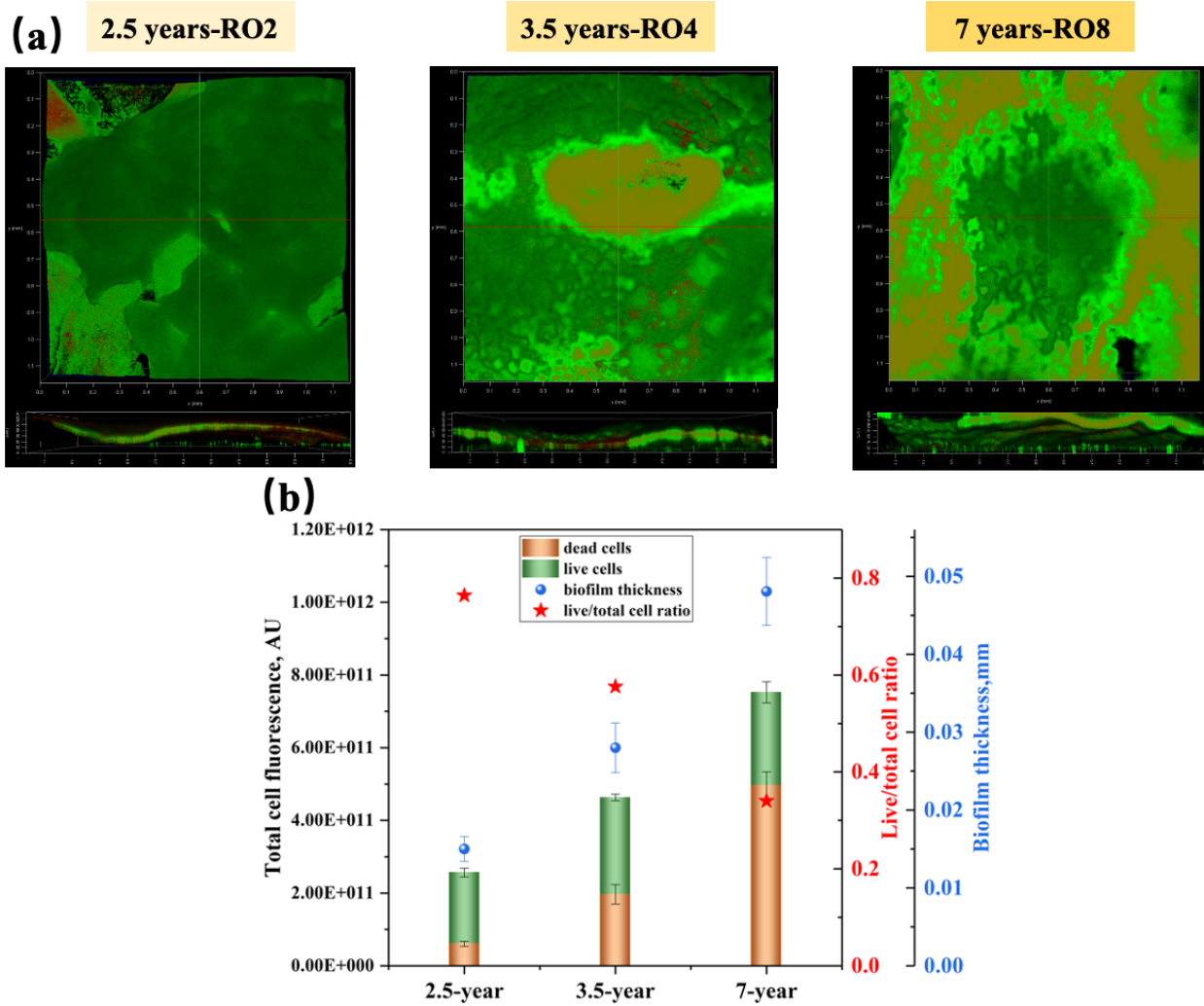
Fig. S2. (a) Confocal laser scanning microscopy (CLSM) orthogonal views, (b) total cell fluorescence (live cells and dead cells) and biofilm thickness of fouled membranes after 2.5, 3.5, and 7 years of operation. (RO2, RO4, and RO8 represent the 2.5, 3.5, and 7-year membranes, respectively).
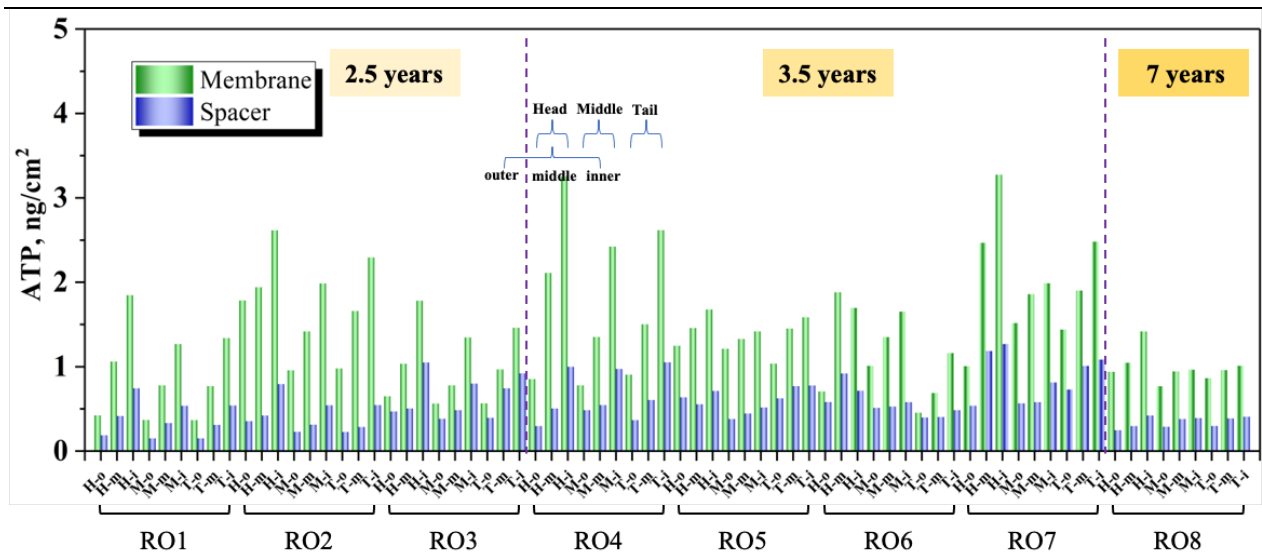
Fig. S3. ATP concentrations on the membrane and feed spacer surfaces after 2.5, 3.5 and 7 years of operation.

Fig. S4. AFM image analysis of the head/inner membrane samples collected from different membrane modules after 2.5, 3.5, and 7 years of operation. (PA represents polyamide virgin membrane).

The AFM images were collected from the head position in the fouled membrane with 2.5, 3.5

and 7 years of operation. A visible difference in the fouled and cleaned membranes was observed (Fig. S4 and Fig. S5). The virgin membrane had wider valleys and a rougher structure, while the fouled membranes had a flatter structure with some protuberances. Over a scanning area of 5 μm × 5 μm, Ra (average roughness, Ra, rms) followed the order virgin membrane (109 nm) > 2.5-year membrane (RO1 (25 nm), RO2 (49.5 nm), and RO3 (61.7 nm)) > 3.5-year membrane (RO4 (80.8 nm), RO5 (81.6 nm), RO6 (72.6 nm), and RO7 (79.5 nm)) > 7-year membrane (RO8 (95 nm)).
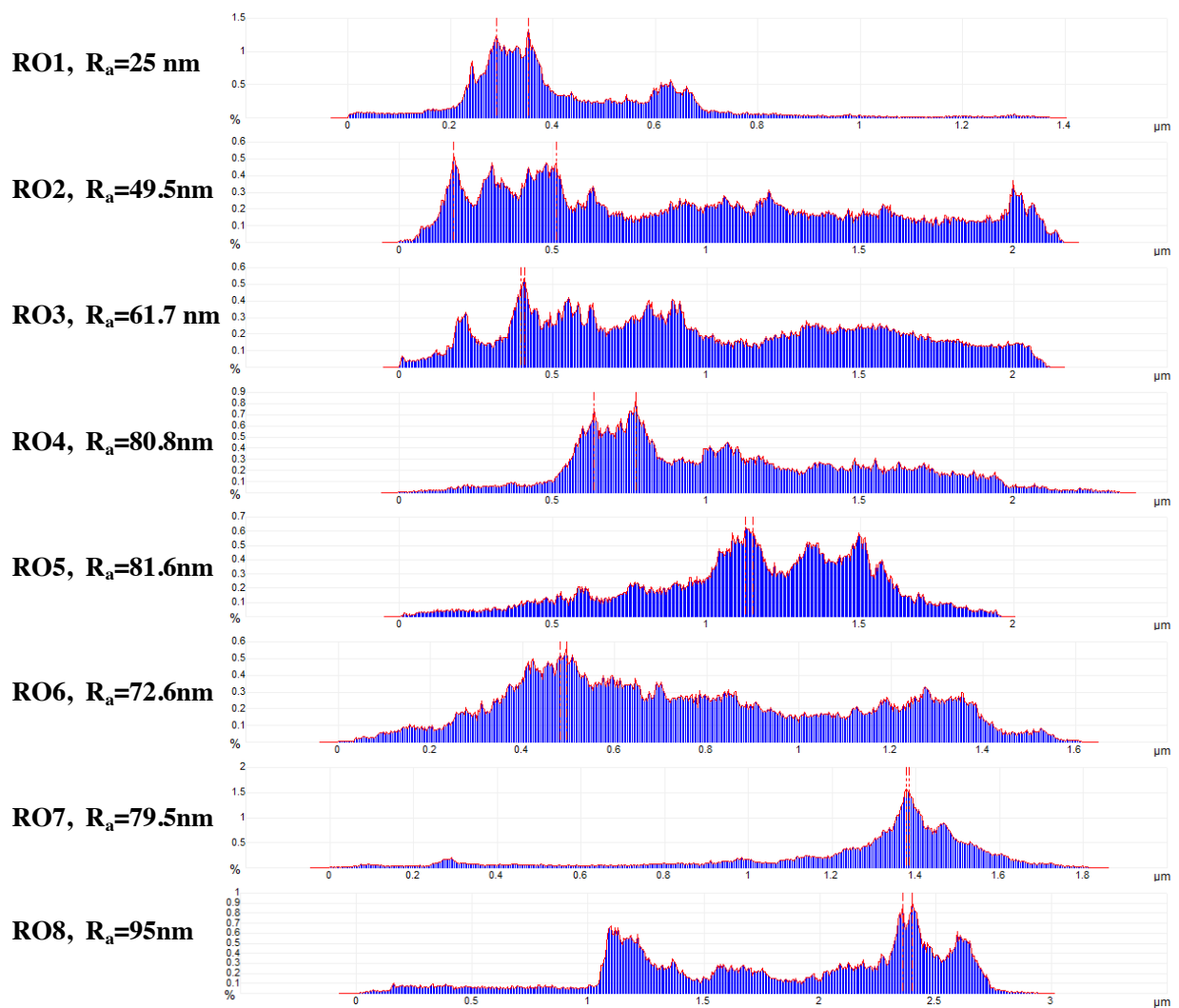
Fig. S5. Distribution of layer thickness from AFM nanoscope analysis of fouled membranes.

(a) Membrane
(b) Spacer
Virgin

(c) Head / Tail
(d) Head / Tail
2.5 years
3.5 years
7 years

(e)
Contact angle, degree
Time, min
Pristine membrane
2.5-year
3.5-year
7-year
7-year
Pristine membrane

(f)
Zeta potential, mV
PA RO1 RO2 RO3 RO4 RO5 RO6 RO7 RO8
2.5 years   3.5 years   7 years
Virgin membrane
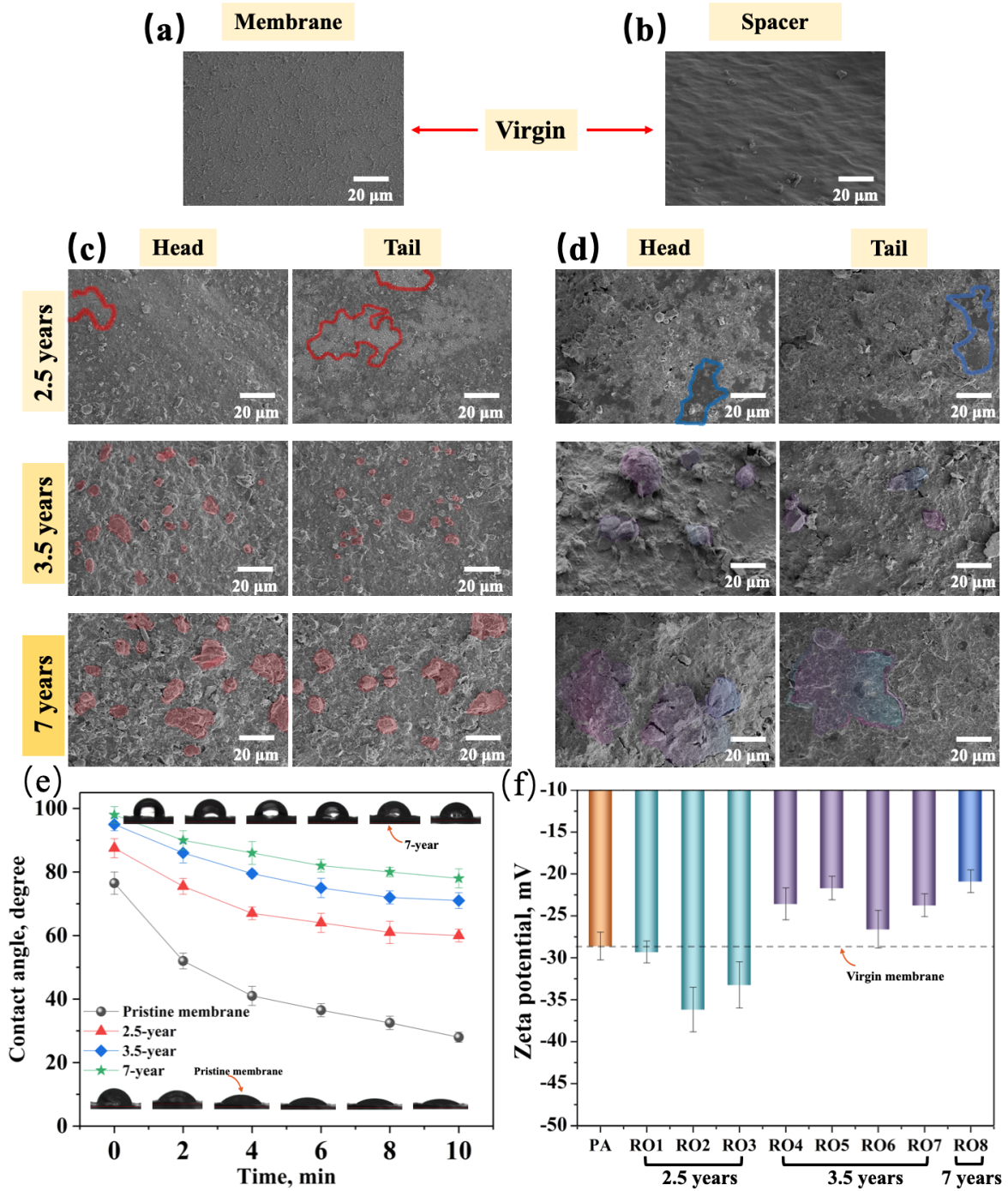
Fig. S6. Scanning electron microscopy (SEM) images of the (a) virgin membrane, (b) spacer, head-tail/inner (c) fouled membrane and (d) spacer samples (RO2, RO4, and RO8 represent the 2.5-year, 3.5-year and 7-year membranes, respectively); (b) contact 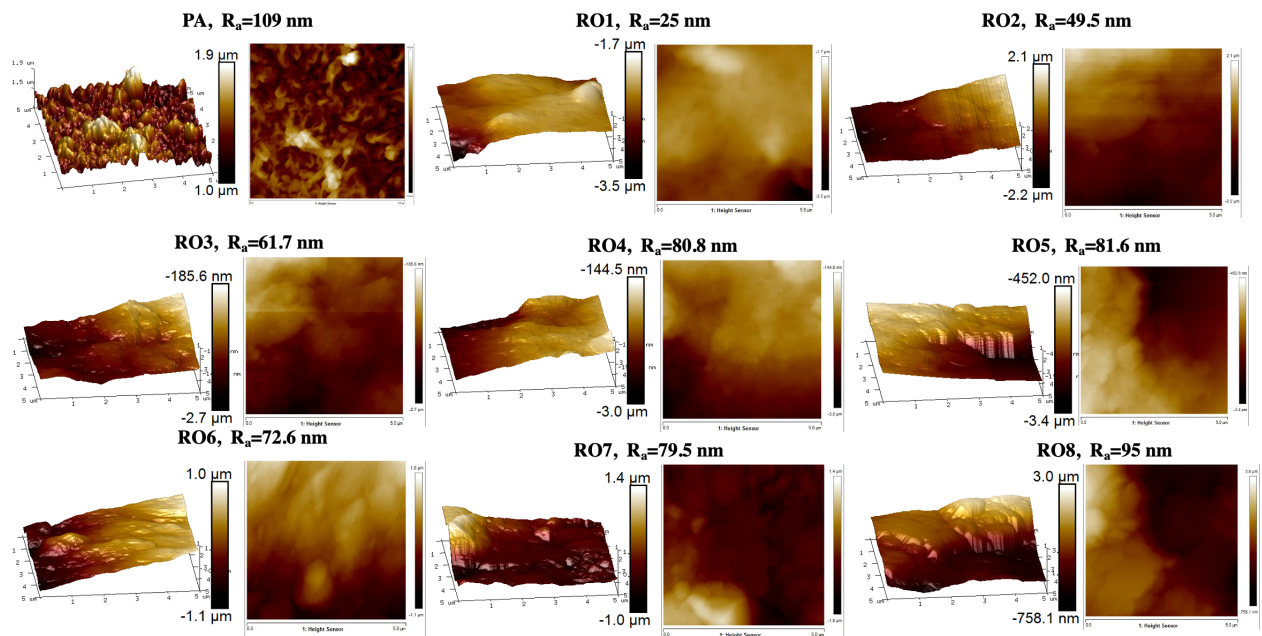angle and (c) zeta potential of the head/inner membrane samples collected from different membrane modules after 2.5, 3.5, and 7 years of operation.

The morphology of fouled membranes and spacers at different operation times was evaluated by SEM. Imaging analysis showed that the virgin membrane surface displayed repeated ridged and valley structures, and the virgin spacer exhibited a flat and smooth structure. A thick heterogeneous foulant layer with a biofilm matrix (Figs. S6c and d), in which irregular particles (indicating inorganic deposition) were embedded, covered the fouled membrane and spacer. Hence, the fouled membrane roughness was lower than that of the virgin membrane (Fig. S4), which could be attributed to the accumulation of EPS and other organics with an adhesive nature that filled the valley and ridge part of the membrane surface (Guo et al., 2022; Jafari et al., 2018).

From the time scale aspect, the surface structure of the virgin membrane and spacer can be observed in the 2.5-year samples (as shown in Fig. S6c and d, where red and blue are circled). This phenomenon might be attributed to frequent membrane cleaning, resulting in the 2.5-year membrane and spacer not being entirely covered by the foulant layer. In contrast, the 3.5-year and 7-year membranes and spacers were covered completely by the foulant layer without the visible features of the virgin membrane. This indicated that a recalcitrant foulant layer had formed on the membrane and spacer with increasing operation time, preventing full recovery of the specific flux upon physicochemical cleaning. Moreover, larger particles and cake-like layers are visible in the

7-year membrane compared to the 2.5-year and 3.5-year membranes, and the accumulation of foulants is distinctive on the membrane and spacer surfaces. Some particles were spherical, which could be caused by inorganic salts such as $CaCO_3$ (Farhat et al., 2018; Qin et al., 2018) according to the inorganic foulant analysis in Fig. 4. From the positional aspect, more particles and fibrils (typical indication of high polysaccharide content (Kweon and Lawler, 2005)) were observed in the samples of head membrane and feed spacer, indicating a relatively high tendency of membrane fouling in the head regions of the module.

The contact angle and zeta potential of the fouled membranes were determined, where the contact angle of the virgin membrane was measured after being compacted with ultrapure water to ensure the consistency of the measurement conditions. The rate of decline of the contact angle of the virgin membrane within 10 min (which decreased 63% to 28°) was more significant than that of the fouled membranes (2.5-year membrane reduced 31% to 60°, 3.5-year membrane reduced 25% to 71°, and 7-year membrane reduced 20% to 78°) (Fig. S6e), suggesting that the wettability of the fouled membrane deteriorates during seawater desalination. The hydrophobicity of the fouled membrane may be attributed to the accumulation of fulvic/humic acid (Carroll et al., 2000; Guo et al., 2009) and protein contents (Mu et al., 2019) with hydrophobic properties on the membrane (Kang and Cao, 2012). As shown in Fig. S6f, the 2.5-year membrane (-32.9 ± 2.36 mV) showed a higher negative charge than the 3.5-year (-22.46 ± 1.73 mV) and 7-year (-26.58 ± 1.35 mV) membranes, which might be due to the higher proportion of live cells (showing higher hydrophilicity and electronegativity than dead cells (Kim et al., 2015)) on the 2.5-year membrane.
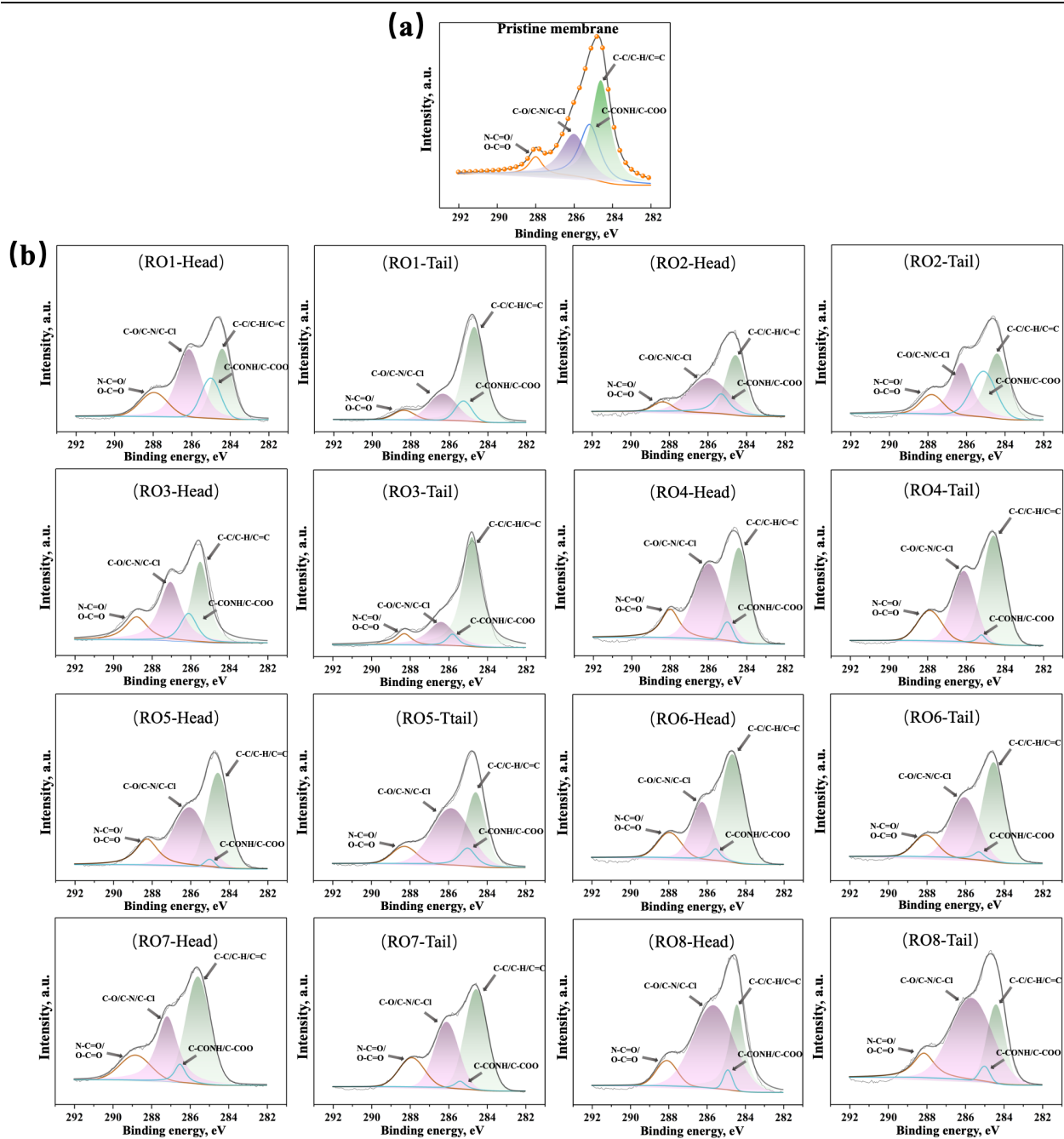
Fig. S7. High-resolution XPS scans for carbon 1s peaks of (a) pristine membrane, and (b) fouled membrane (lead and tail samples).
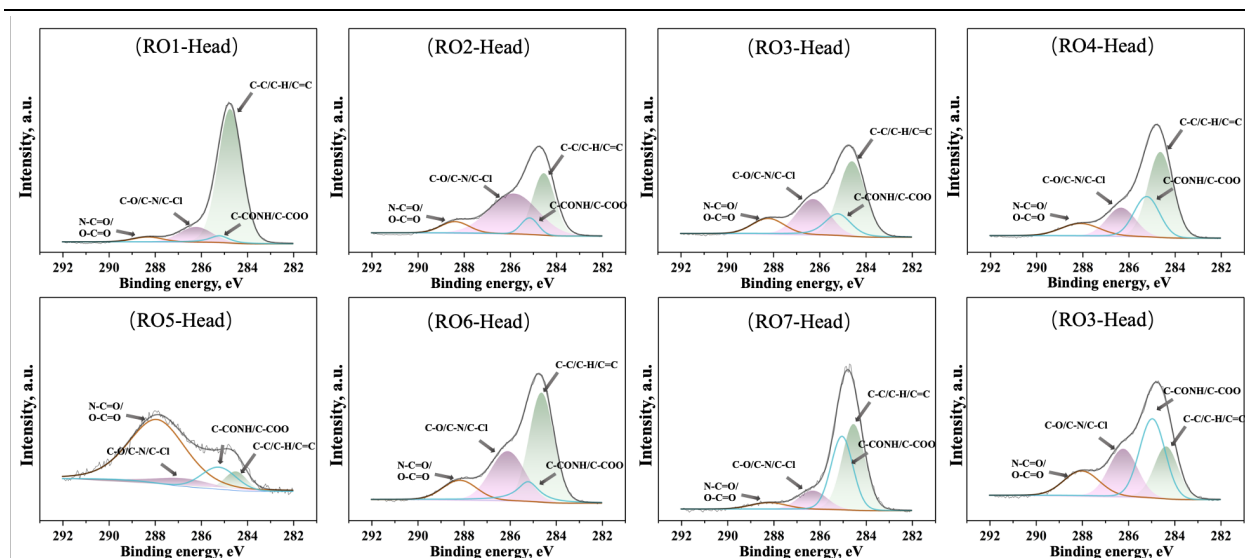
Fig. S8. High-resolution XPS scans for carbon 1s peaks of the fouled feed spacer.
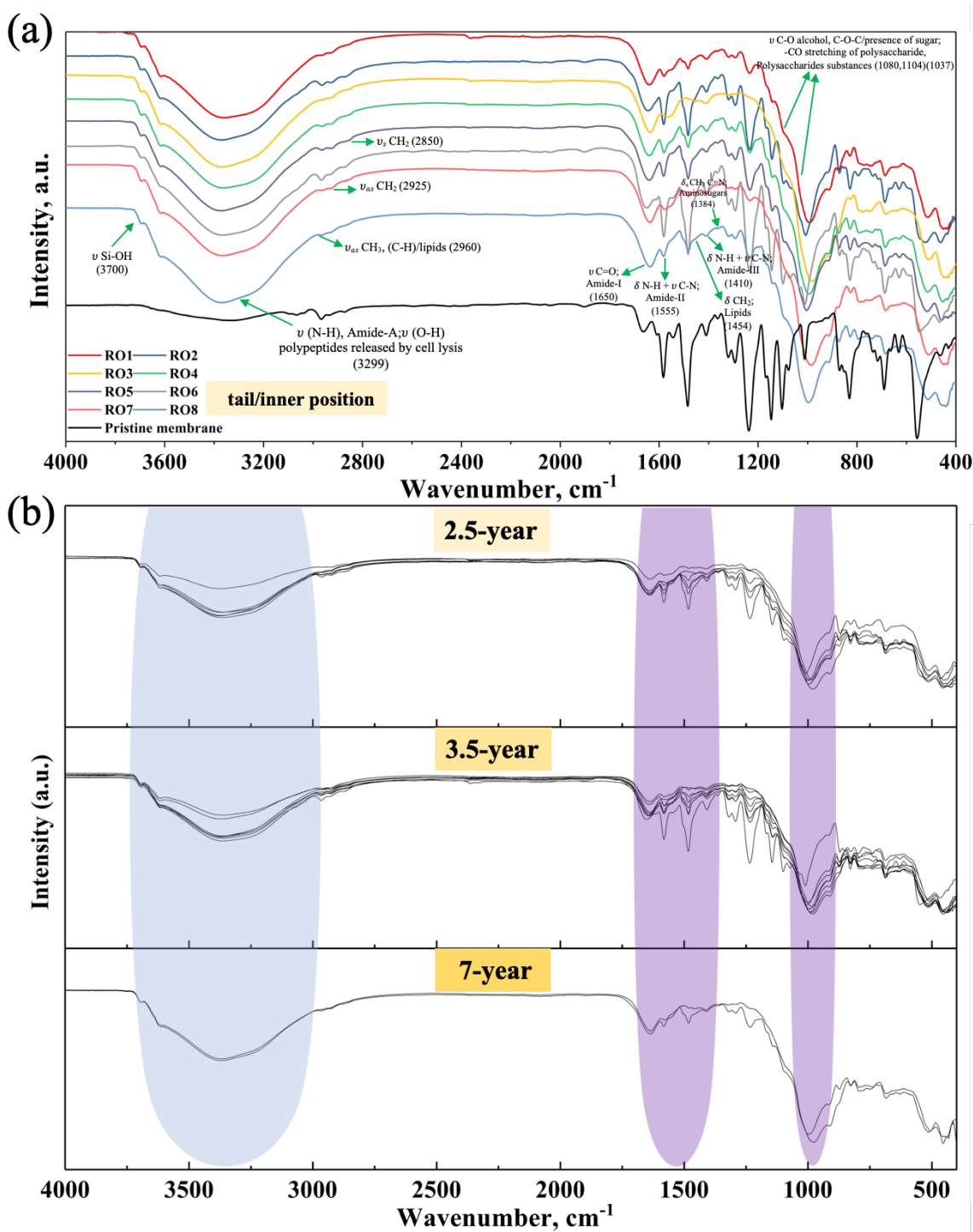
Fig. S9. ATR-FTIR spectral vibrations and peak assignments of the functional groups within the fouling layer on the (a) tail/inner membranes after (b) 2.5, 3.5, and 7 years of operation.

Several bands at lower wavenumbers exhibit lower intensity on the fouled membrane than on the pristine membrane, most notably between 1600 and 1050 cm^{-1} and between 900 and 500 cm^{-1}.

This is attributed to the fact that the foulant covering the membrane prevents adsorption by the pristine membrane material in the infrared region. The fouled membranes showed characteristic peaks at 3299, 1650, 1555, 1410, and 1037 cm^{-1}, suggesting the existence of amide-A (N-H stretching vibration), amide-I (mainly C=O stretching vibration), amide-II, amide-III (N-H bending and C-N stretching vibrations) (Khan et al., 2014), and polysaccharides on the membrane. The spectra of the fouled membrane also exhibit absorption bands at approximately 870 and 3700 cm^{-1}, indicating the existence of carbonates and Si-OH (stretching) formation on the membrane (Lee and Kim, 2009). ICP–OES analysis of the inorganic components of the foulant layer also supports this conclusion. Several peaks (3299 cm^{-1} and 1037 cm^{-1}) of higher intensity are observed for the 7-year membrane than the 2.5- and 3.5-year membranes, suggesting relatively higher occurrences of fouling on the 7-year membrane.

Fig. S10. Alpha and beta diversity comparisons of microbial communities at the operational taxonomic unit (OTU) level. Shown are Student's test for (a) Chao index and (b) Shannon corresponding to alpha diversity; combined plot integrated with the (c) PLS-DA and (d) PCoA plots of the bacterial communities corresponding to beta diversity; (e) Venn diagram of core OTUs in membrane biofilms developed after 2.5, 3.5, and 7 years of operation. Biofilm were collected from head/inner and tail/inner membrane samples.

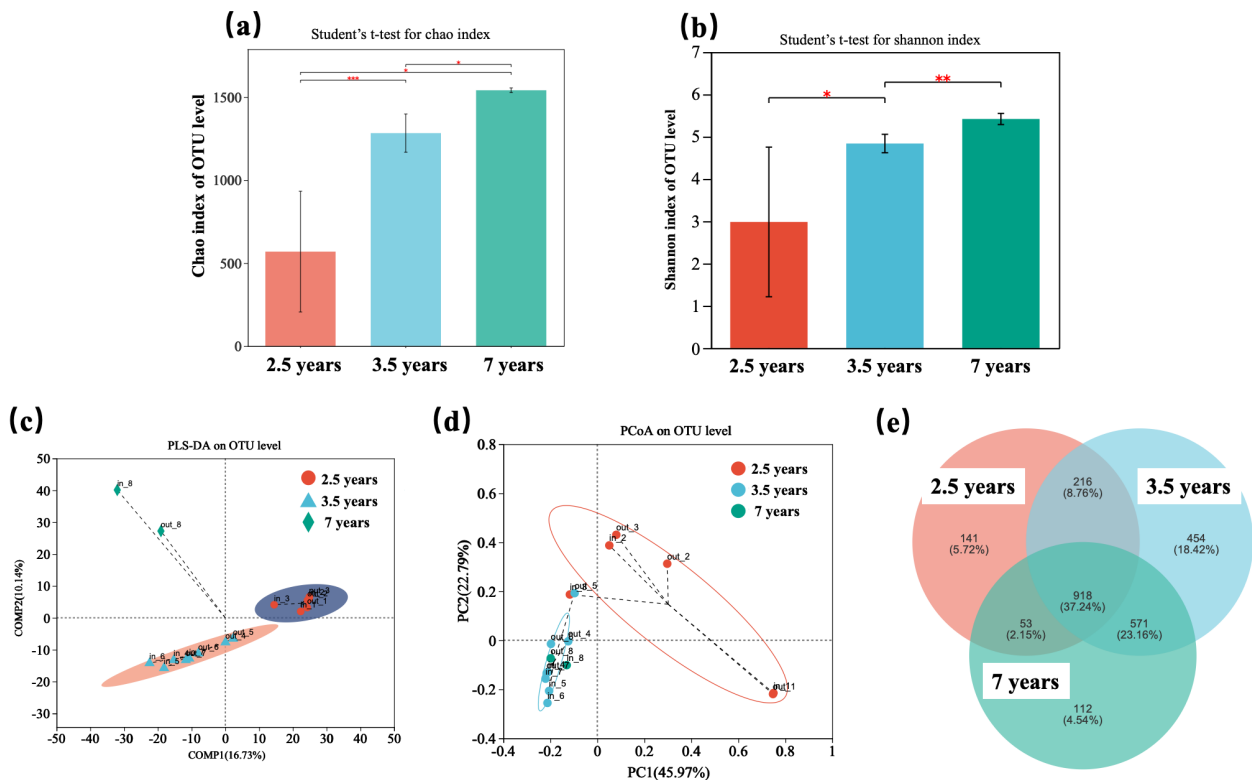To characterize the microbial communities in SWRO membrane biofouling, we conducted 16S rRNA gene high-throughput sequencing. Each group demonstrated a high coverage index (>0.99) (Table. S3), ensuring high credibility and accurate representation of the microbial community. Alpha-diversity estimators (Ace, Chao, Shannon, and Simpson) are presented in Figs. S10(a and b) and Table. S2. The microbial richness was expressed by the Ace and Chao indices (Table. S2 and Fig. S10a), which were higher in the 7-year group (1563.5 and 1541.9) than in the 2.5-year group (583.26 and 569.47) and 3.5-year group (1291.5 and 1283.6). The diversity and evenness of the microbial community were expressed by the Shannon and Simpson values (Wang et al., 2020). The highest Shannon value of 5.4178 and the lowest Simpson value of 0.012868 were observed in the 7-year group, while the 2.5-year group (2.9823 and 0.2812) and the 3.5-year group (4.8372 and 0.024781) had lower values (Fig. S10b).

In terms of beta diversity (Figs. S10c and d), partial least squares discriminant analysis (PLS-DA) (Figs. S10c) showed no overlaps between the clusters of the three sample groups, signifying changes in the microbial community with increasing operation time. Based on the operational taxonomic unit (OTU) results at the normalized sequencing depth, the Venn diagram revealed that

918 OTUs were shared among these three groups (Fig. S10e), representing the core microorganisms of biofouling on the SWRO membrane. The Bray–Curtis distance-based principal coordinate analysis (PCoA) (Fig. S10d) showed that the data points of the 7-year group were closer to those of the 3.5-year group than to those of the 2.5-year group. Specifically, there were 1,489 common OTUs between the 7-year and 3.5-year groups (Fig. S10e) and 971 common OTUs between the 7-year and 2.5-year groups, indicating that the microbial composition of the 7-year group was more similar to that of the 3.5-year group than to that of the 2.5-year group.
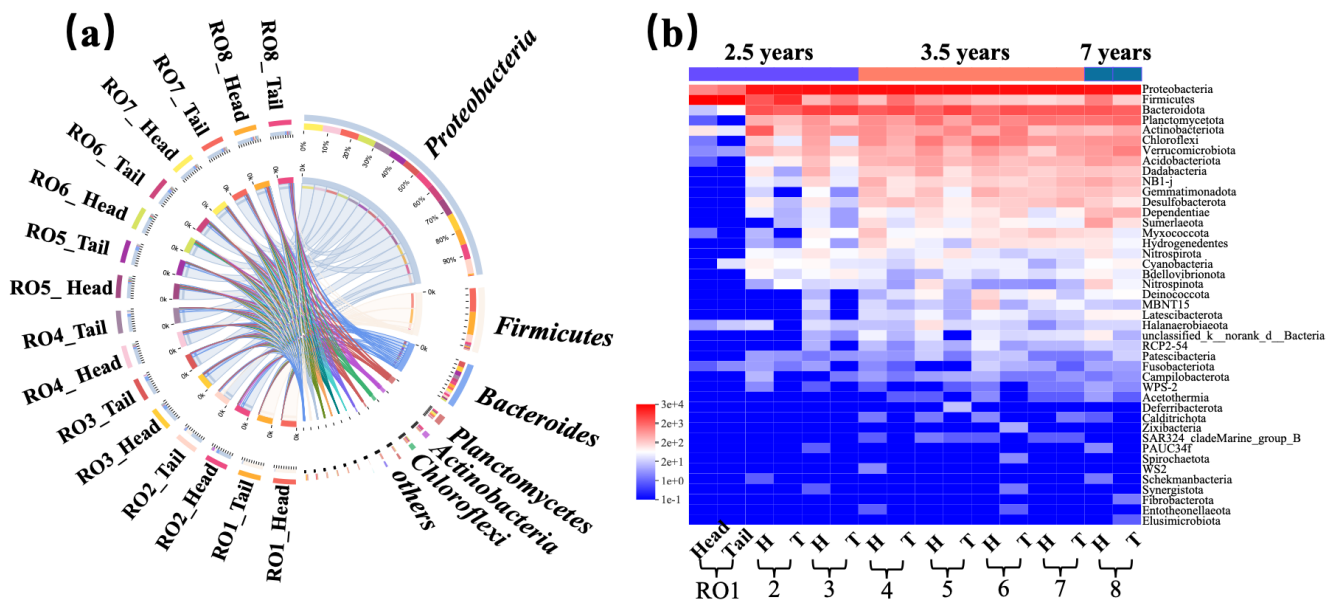

Fig. S11. Multivariate analysis of the sequence dataset. (a) Circos map of the phylum-level composition of the membrane samples at different locations, and (b) heatmap of the phylum-level composition of the membrane samples at different locations.
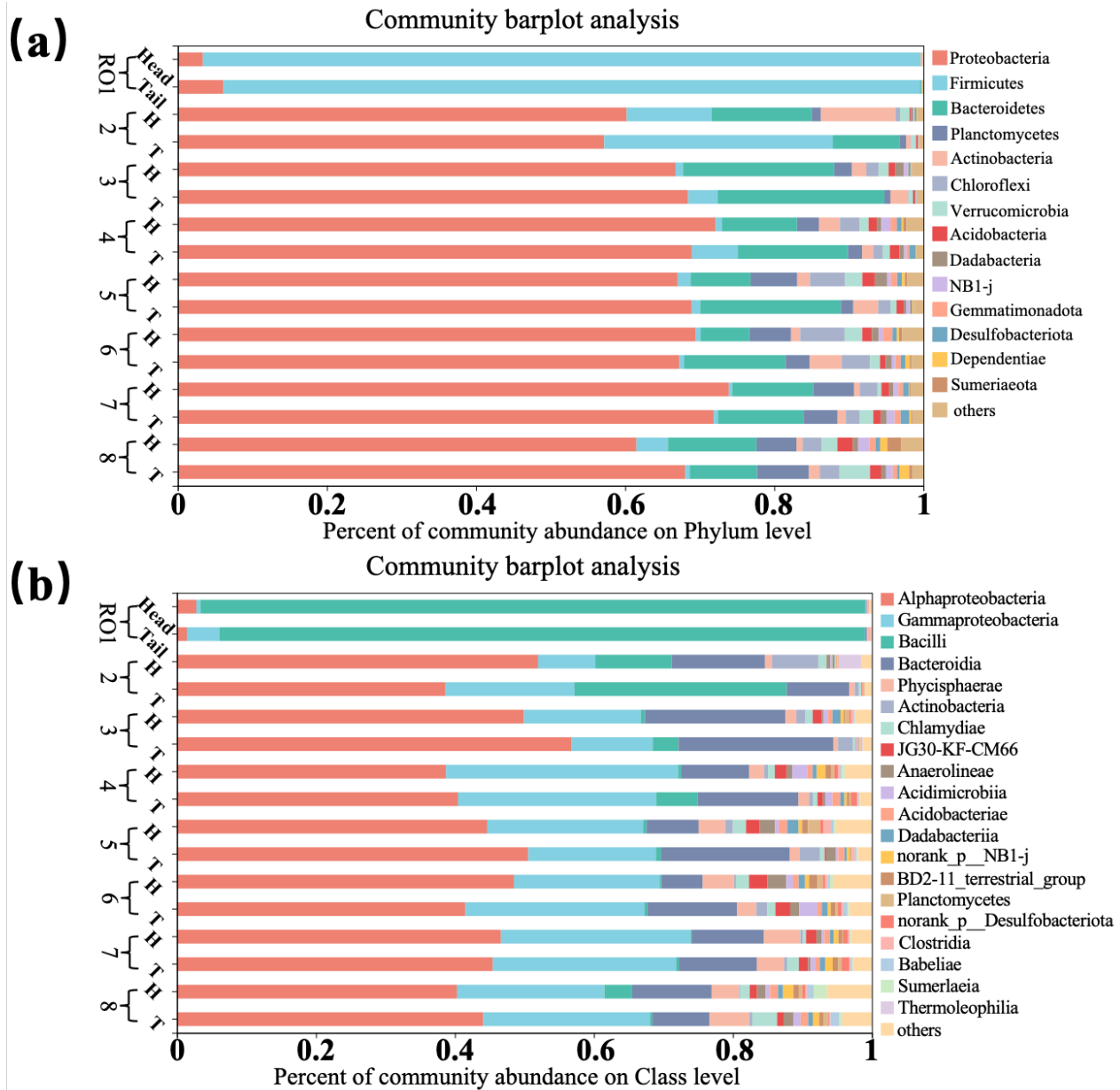
Fig. S12. Multivariate analysis of the sequence dataset. Relative abundance of dominant bacteria at the (a) phylum and (b) class levels.
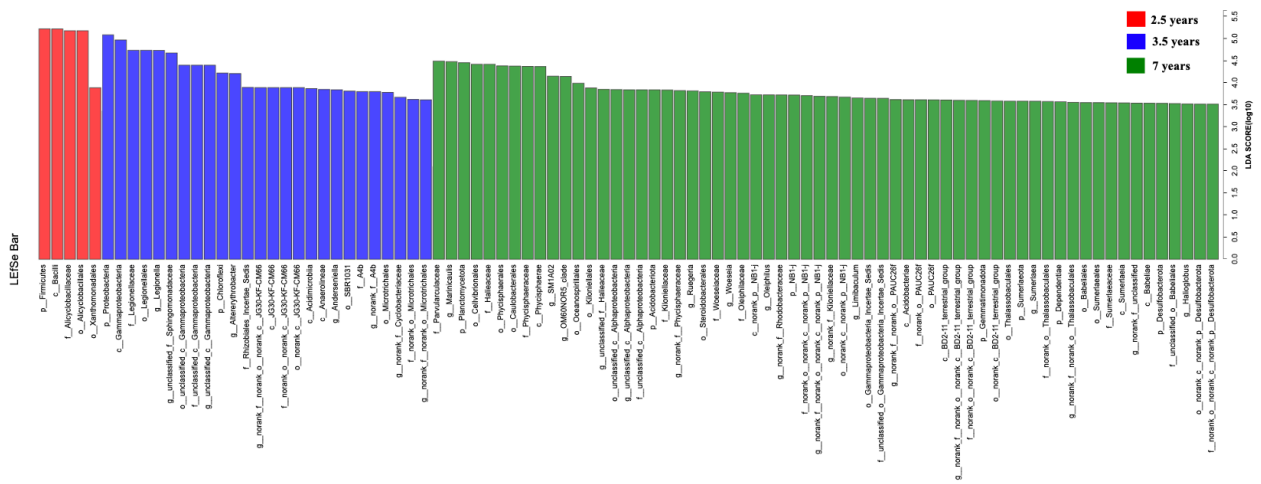
Fig. S13. LEfSe analysis of microbial abundance with a bar chart of LDA score.

To explore the classified bacterial taxa with significant abundance differences among the three experimental groups, we performed biomarker analysis using the linear discriminant analysis (LDA) effect size (LEfSe) method (Liu et al., 2020). As displayed in the LEfSe bar chart (Fig. S13), most bacteria exhibited an abundance advantage in the 7-year group (49 clades), while relatively fewer clades were distinctly enriched in the 2.5-year group (5 clades) and 3.5-year group (26 clades). Specifically, three biomarkers with higher LDA_values (over 3.5) in the 2.5-year group were *Bacilli* (class), and *Alicyclobacillaceae* (family) belonging to *Firmicutes* (phylum), and *Xanthomonadales* (order) belonging to *Proteobacteria* (phylum). In the 3.5-year group, the membrane was primarily occupied by members of *Gammaproteobacteria* (class), *Legionellaceae* (family), *Legionellales* (order), *Legionella* (genus), and *Sphingomonadaceae* (family), which belonged to *Proteobacteria* (phylum). In comparison, the 7-year group was prevailingly enriched by several biomarkers of *Parvularculaceae* (family), *Marinicaulis* (genus), *Cellvibrionales* (order), *Halieaceae* (family), *Caulobacterales* (order), *Phycisphaerales* (order), *Phycisphaeraceae*

24

(family), *Phycisphaerae* (class), and *SM1A02* (genus), belonging to *Proteobacteria* (phylum) and *Planctomycetes* (phylum). LEfSe obviously revealed that the biomarkers were significantly different among these three groups, wherein most biomarkers belonging to *Firmicutes* appeared in the 2.5-year group, and the 3.5- and 7-year groups were obviously enriched by several biomarkers belonging to *Proteobacteria* and *Planctomycetes*.

Fig. S14. Water flux and salt rejection for the pristine and used membranes.

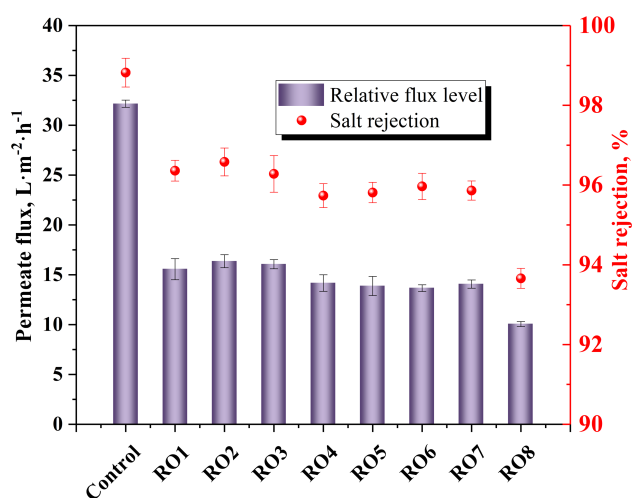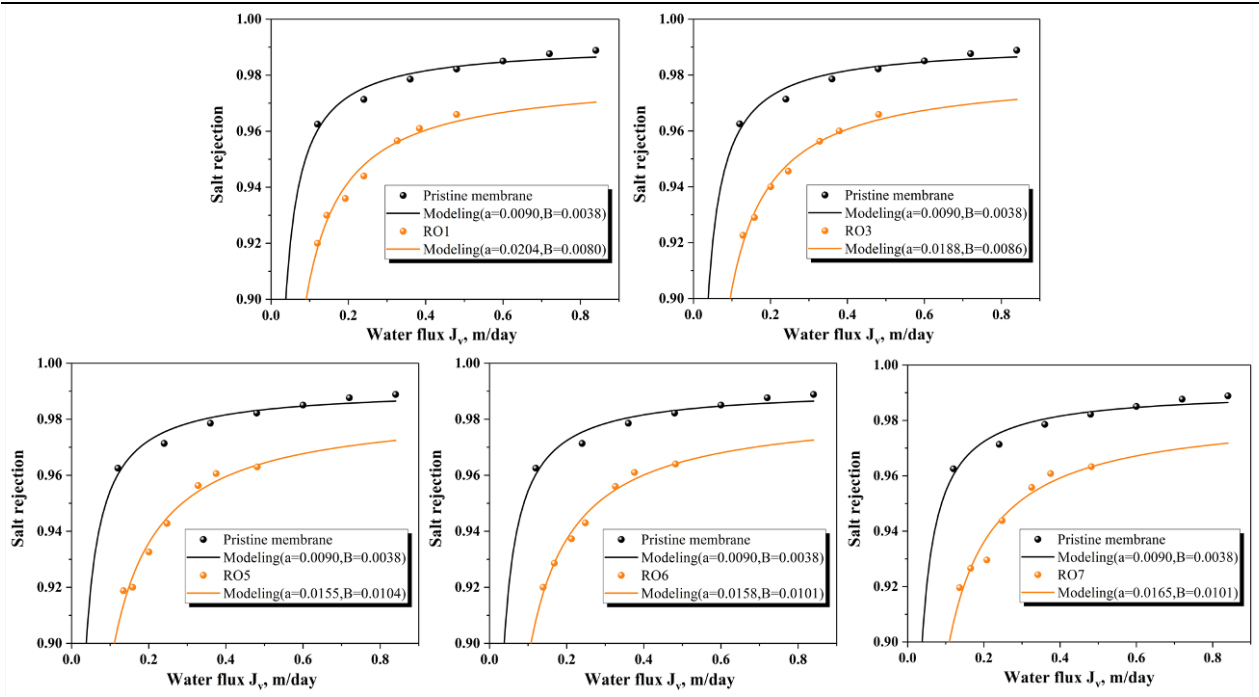**Fig. S15.** Water flux and salt rejection for the pristine and used membranes (RO1, RO3, RO5, RO6, and RO7). Eqs. (S1) and (S4) were used for the modeling of water flux and salt rejection. Coefficients (with 95% confidence bounds). Symbols and lines represent experimental data and model fit, respectively.
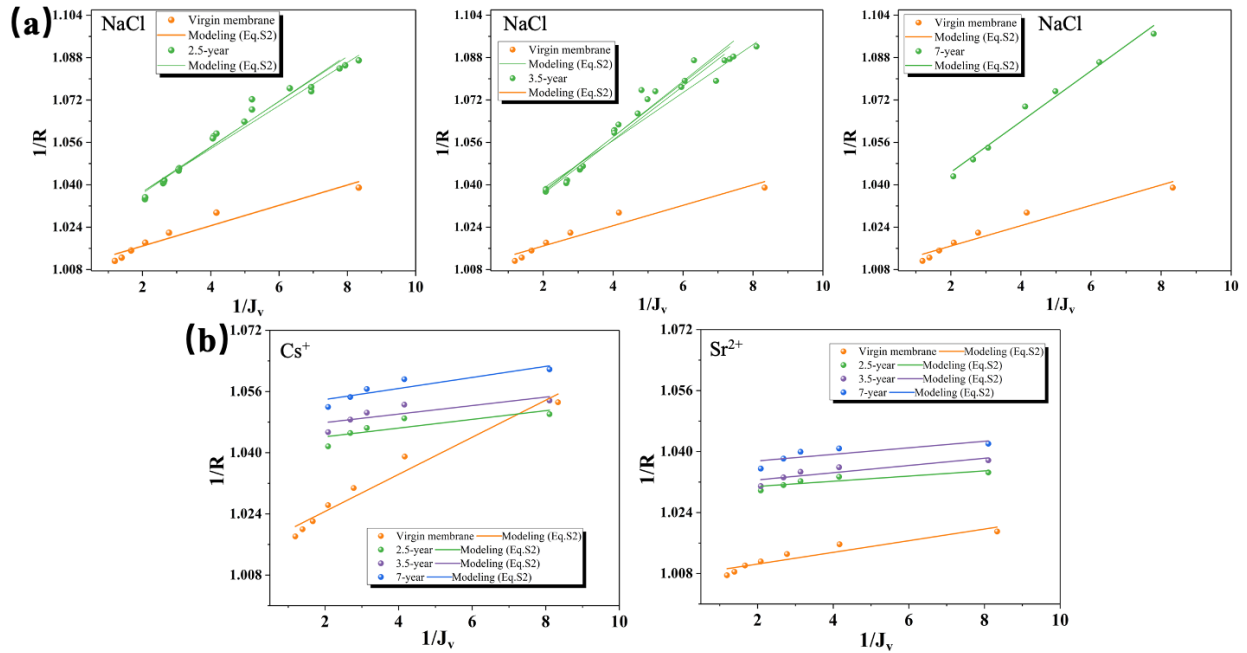
Fig. S16. Solute rejection ((a) NaCl and (b) Cs^+ and Sr^{2+}) for the pristine and used membranes. Symbols and lines represent experimental data and model fit, respectively.

Fig. S16 shows our experimental results modeled using Eq. (S6). The results indicate that Eq. (S6) describes the experimental results well, which shows that $exp\left(\frac{J_v}{k}\right) \approx 1$ in our experiments.

Table S1. Average of raw seawater, feed water and permeate water quality characteristics (from 2020 to 2021).

Parameter	Unit	Raw seawater	1st RO influent	Water supply parameter
Conductivity	$mS \cdot cm^{-1}$	45.9	46	0.771
pH	-	8.1	8.1	7.6
Turbidity	NTU	5.8	<0.2	-
Boron	$mg \cdot L^{-1}$	4.2	-	0.9
TSS	$mg \cdot L^{-1}$	11.5	-	-
COD	$mg \cdot L^{-1}$	1.53	<1.5	-
NH_3-N	$mg \cdot L^{-1}$	0.06	-	-
UV_{254}	cm^{-1}	3	-	-
TDS	$mg \cdot L^{-1}$	29450	-	522
Hardness	$mg \cdot L^{-1} CaCO_3$	5800	-	64.0
Basicity	$mg \cdot L^{-1} CaCO_3$	118.09	-	30.0
SDI	-	-	<3	-

Table S2. Analytical methods and descriptions.

Analysis categories	Methods	Descriptions	References
Organic biometabolic components	Bradford method (BCA Protein Assay Kit, Thermo Scientific, USA), phenol-H_2SO_4 method and TOC-VCSH analyzer (Shimadzu, Boulder, CO, USA)	Organic biometabolic components were extracted using NaOH solution (1 M) to measure extracellular polymeric substances (EPS, protein and polysaccharide) and total organic carbon (TOC)	(Li et al., 2018)
	Excitation-emission matrix (EEM) analysis (F-4600, Hitachi, Japan)	EEM was performed to identify the fluorescent substances	(Yu et al., 2010)

Inorganic components	ICP–OES (Perkin Elmer OPTIMA 7300 V)	Inorganic foulants were extracted in an acid solution of 1:1 (v/v) MQ:pure HNO_3 (70%) to measure the inorganic ions	(Fortunato et al., 2020)
Microbial analysis	BacTiter-Glo microbial viability assay kit (Promega, USA)	Adenosine triphosphate (ATP) content	(Li et al., 2018)
	SYTO9 and propidium iodide (LIVE/DEAD Baclight Bacterial Viability Kit, Life Technologies Corporation)	live, dead cells measurements	(Li et al., 2018)
	Next-generation sequencing of the 16S ribosomal RNA gene	Microbial community analysis on the fouled membrane	(Liu et al., 2020)
Fouled membrane characterization	Contact angle analyzer (JC2000D2, China)	The contact angle measurement of the fouled membrane	(Lin et al., 2020)
	Electrokinetic analyzer (Anton Paar, GmbH)	The Zeta potential measurement of the fouled membrane	(Lin et al., 2020)
	Field emission scanning electron microscopy (FESEM, HITACHI S-4800) and BRUKER	The morphologies characterization of the fouled membrane and spacer	(Abada et al., 2022)
	Dimension icon atomic force microscopy (AFM)	The morphologies characterization of the fouled membrane	(Zhu et al., 2018)
	FTIR spectrometer (TENSOR 27, BRUKER)	Functional group analyses of the fouled membrane	(Abada et al., 2022)
	X-ray photoelectron spectroscopy (XPS, ESCSLAB 250Xi)	Functional group analyses of the fouled membrane and spacer	(Gorzalski et al., 2017)
Permeation evaluation	Conductivity meter (DDSJ-319L) and inductively coupled plasma–mass spectroscopy (ICP–MS) analysis (Shimadzu ICP–MS 2030)	The concentration of salt was obtained by a conductometer, and the Cs^+ and Sr^{2+} concentrations were measured	(Suzuki et al., 2016)

Statistical analyses	Phylogenetic molecular ecological networks (pMENs) and Spearman correlation analysis	pMENs and heatmap factor analysis were conducted to decipher the real culprit of biofouling in the practical application.	(Jo et al., 2016; Zhu et al., 2022)
	Redundancy analysis (RDA) using CANOCO5 software	The relationships between fouling results (solute rejection and membrane flux decline) and fouling factors (organic, inorganic, and biological foulants) on the membrane surface was studied	(Lin et al., 2019)
	Variance partitioning analysis (VPA) coupled with multiple linear regression	The individual and interactive contributions of fouling factors (organic, inorganic, and biological foulants) to membrane fouling were quantitatively evaluated	(Lin et al., 2019)

Table S3. Sequencing data summary and community diversity

	2.5-year	3.5-year	7-year	P-value (2.5-3.5)	P-value (2.5-7)	P-value (3.5-7)
Sobs	478	1036.8	1292	0.0003992	0.01232	0.0129
Shannon	2.9823	4.8372	5.4178	0.0116	0.1146	0.007948
Simpson	0.2812	0.024781	0.012868	0.06889	0.3658	0.05563
Ace	583.29	1291.5	1563.5	0.0002314	0.01221	0.00993
Chao	569.47	1283.6	1541.9	0.000197	0.01158	0.01628
Coverage	0.99611	0.9911	0.99373	0.0001502	0.01281	0.06756

References

Abada, B., Safarik, J., Ishida, K.P. and Chellam, S. 2022. Surface characterization of end-of-life reverse osmosis membranes from a full-scale advanced water reuse facility: Combined role of bioorganic materials and silicon on chemically irreversible fouling. J Membrane Sci 653.

Belila, A., El-Chakhtoura, J., Otaibi, N., Muyzer, G., Gonzalez-Gil, G., Saikaly, P.E., van Loosdrecht, M.C.M. and Vrouwenvelder, J.S. 2016. Bacterial community structure and variation in a full-scale seawater desalination plant for drinking water production. Water Res 94, 62-72.

Carroll, T., King, S., Gray, S.R., Bolto, B.A. and Booker, N.A. 2000. The fouling of microfiltration membranes by NOM after coagulation treatment. Water Res 34(11), 2861-2868.

Edgar, R.C. 2013. UPARSE: highly accurate OTU sequences from microbial amplicon reads. Nat Methods 10(10), 996-+.

Farhat, S., Bali, M. and Kamel, F. 2018. Membrane autopsy to provide solutions to operational problems of Jerba brackish water desalination plant. Desalination 445, 225-235.

Fortunato, L., Alshahri, A.H., Farinha, A.S.F., Zakzouk, I., Jeong, S. and Leiknes, T. 2020. Fouling investigation of a full-scale seawater reverse osmosis desalination (SWRO) plant on the Red Sea: Membrane autopsy and pretreatment efficiency. Desalination 496.

Gorzalski, A.S., Donley, C. and Coronell, O. 2017. Elemental composition of membrane foulant layers using EDS, XPS, and RBS. J Membrane Sci 522, 31-44.

Guo, S.J., Li, J.F., Ren, J., Zhao, H.Z. and Cheng, F.Q. 2022. Membrane fouling of raw coking wastewater in membrane distillation: Identification of fouling potential of hydrophilic and hydrophobic components. Desalination 539.

Guo, X.Y., Li, Q.L., Hu, W.L., Gao, W. and Liu, D.F. 2009. Ultrafiltration of dissolved organic matter in surface water by a polyvinylchloride hollow fiber membrane. J Membrane Sci 327(1-2), 254-263.

Jafari, M., Desmond, P., van Loosdrecht, M.C.M., Derlon, N., Morgenroth, E. and Picioreanu, C. 2018. Effect of biofilm structural deformation on hydraulic resistance during ultrafiltration: A numerical and experimental study. Water Res 145, 375-387.

Jo, S.J., Kwon, H., Jeong, S.Y., Lee, C.H. and Kim, T.G. 2016. Comparison of microbial communities of activated sludge and membrane biofilm in 10 full-scale membrane bioreactors. Water Res 101, 214-225.

Kang, G.D. and Cao, Y.M. 2012. Development of antifouling reverse osmosis membranes for water treatment: A review. Water Res 46(3), 584-600.

Khan, M.T., Busch, M., Molina, V.G., Emwas, A.H., Aubry, C. and Croue, J.P. 2014. How different is the composition of the fouling layer of wastewater reuse and seawater desalination RO membranes? Water Res 59, 271-282.

Kim, L.H., Shin, M.S., Kim, S.J., Kim, C.M., Chae, K.J. and Kim, I.S. 2015. Potential effects of damaged Pseudomonas aeruginosa PAO1 cells on development of reverse osmosis membrane biofouling. J Membrane Sci 477, 86-92.

Kweon, J.H. and Lawler, D.F. 2005. Investigation of membrane fouling in ultrafiltration using model organic compounds. Water Sci Technol 51(6-7), 101-106.

Lee, M. and Kim, J. 2009. Membrane autopsy to investigate CaCO3 scale formation in pilot-scale, submerged membrane bioreactor treating calcium-rich wastewater. J Chem Technol Biot 84(9), 1397-1404.

Li, C., Liang, J., Yang, Y., Pu, J. and Hou, L.A. 2018. Novel insights into the role of Pseudomonas quinolone signal in the control of reverse osmosis membrane biofouling. J Membrane Sci 563, 505-512.

Lin, W.C., Li, M.C., Wang, Y.H., Wang, X.M., Xue, K., Xiao, K. and Huang, X. 2019. Quantifying the dynamic evolution of organic, inorganic and biological synergistic fouling during nanofiltration using statistical approaches. Environ Int 133.

Lin, W.C., Li, M.C., Xiao, K. and Huang, X. 2020. The role shifting of organic, inorganic and biological foulants along different positions of a two-stage nanofiltration process. J Membrane Sci 602.

Liu, C., Zhu, L. and Chen, L. 2020. Effect of salt and metal accumulation on performance of membrane distillation system and microbial community succession in membrane biofilms. Water Res 177, 115805.

Lozupone, C., Lladser, M.E., Knights, D., Stombaugh, J. and Knight, R. 2011. UniFrac: an effective distance metric for microbial community comparison. Isme Journal 5(2), 169-172.

Ma, L., Yang, Y., Liu, W.H. and Bu, D.P. 2023. Sodium butyrate supplementation impacts the gastrointestinal bacteria of dairy calves before weaning. Appl Microbiol Biot 107(10), 3291-3304.

Matthiasson, E. and Sivik, B. 1980. Concentration Polarization and Fouling. Desalination 35(1-3), 59-103.

Mu, S.T., Wang, S., Liang, S., Xiao, K., Fan, H.J., Han, B.J., Liu, C., Wang, X.M. and Huang, X. 2019. Effect of the relative degree of foulant "hydrophobicity" on membrane fouling. J Membrane Sci 570, 1-8.

Qin, W.L., Xie, Z.L., Ng, D., Ye, Y., Ji, X.S., Gray, S. and Zhang, J.H. 2018. Comparison of colloidal silica involved fouling behavior in three membrane distillation configurations using PTFE membrane. Water Res 130, 343-352.

Stedmon, C.A. and Bro, R. 2008. Characterizing dissolved organic matter fluorescence with parallel factor analysis: a tutorial. Limnol Oceanogr-Meth 6, 572-579.

Suzuki, T., Tanaka, R., Tahara, M., Isamu, Y., Niinae, M., Lin, L., Wang, J.B., Luh, J. and Coronell, O. 2016. Relationship between performance deterioration of a polyamide reverse osmosis membrane used in a seawater desalination plant and changes in its physicochemical properties. Water Res 100, 326-336.

Urama, R.I. and Marinas, B.J. 1997. Mechanistic interpretation of solute permeation through a fully aromatic polyamide reverse osmosis membrane. J Membrane Sci 123(2), 267-280.

Wang, H., Liu, Z.W., Luo, S., Khan, R., Dai, P., Liang, P., Zhang, X.Y., Xiao, K. and Huang, X. 2020. Membrane autopsy deciphering keystone microorganisms stubborn against online NaOCl cleaning in a full-scale MBR. Water Res 171.

Wu, B.R., Dai, X.H. and Chai, X.L. 2020. Critical review on dewatering of sewage sludge: Influential mechanism, conditioning technologies and implications to sludge re-utilizations. Water Res 180.

Xu, B., Cho, Q.A.C., Ng, T.C.A., Huang, S. and Ng, H.Y. 2022. Enriched autoinducer-2 (AI-2)-based quorum quenching consortium in a ceramic anaerobic membrane bioreactor (AnMBR) for biofouling retardation. Water Res 214, 118203.

Yu, G.H., He, P.J. and Shao, L.M. 2010. Novel insights into sludge dewaterability by fluorescence excitation-emission matrix combined with parallel factor analysis. Water Res 44(3), 797-806.

Zhu, R.C., Diaz, A.J., Shen, Y., Qi, F., Chang, X.M., Durkin, D.P., Sun, Y.X., Solares, S.D. and Shuai, D.M. 2018. Mechanism of humic acid fouling in a photocatalytic membrane system. J Membrane Sci 563, 531-540.

Zhu, X.Z., Lee, L.W., Song, G.Q., Zhang, X., Gao, Y., Yang, G., Luo, S. and Huang, X. 2022. Deciphering mono/multivalent draw solute-induced microbial ecology and membrane fouling in anaerobic osmotic membrane bioreactor. Water Res 209.